Available online at www.sciencedirect.com

ScienceDirect

Ceramics International 40 (2014) 591–603

CERAMICS INTERNATIONAL

www.elsevier.com/locate/ceramint

Effects of prestrain applied to poly(ethylene terephthalate) substrate before coating of indium–tin–oxide film on film quality and optical, electrical, and mechanical properties

Tse-Chang Li[a], Chung-Jen Chung[b], Chang-Fu Han[a], Po-Tsung Hsieh[b], Kuan-Jen Chen[c], Jen-Fin Lin[a,b,*]

[a]Department of Mechanical Engineering, National Cheng Kung University, Tainan 701, Taiwan
[b]Center for Micro/Nano Science and Technology, National Cheng Kung University, Tainan 701, Taiwan
[c]The Instrument Center, National Cheng Kung University, Tainan 701, Taiwan

Received 24 May 2013; received in revised form 13 June 2013; accepted 13 June 2013
Available online 20 June 2013

Abstract

Four kinds of poly(ethylene terephalate) (PET)/indium–tin–oxide (ITO) specimen were prepared to examine the effect of prestrain applied to the PET substrate before the coating of ITO film on the mechanical, microstructure, optical, and electrical properties and morphology. The dependence and interaction among these properties/parameters are established and discussed. The mean slenderness ratio of the crystalline porosities in the ITO film decreased with increasing prestrain. The tilt angle of tubular porosities increased due to the increase in the particle size of ITO deposited on the PET substrate. A nonzero prestrain reduced both interplanar spacing (d-spacing) and the mean surface roughness of the ITO film. An increase in the substrate prestrain decreased the mean transmittance but increased the mean reflectance of the specimens. An increase in the ITO particle size lowered the optical band gap (*Eg*) and mean reflection and increased the mean transmittance. PET/ITO specimens with larger *Eg* values had higher carrier mobility (*Mb*). A nonzero prestrain leads to a smooth ITO film with low electrical resistance. Decreasing Young's modulus in combination with increasing specimen's hardness is helpful to the increase in the pop-in depth and the decrease in the pop-out depth in the nanoindentations. The electrical current–depth curve from nanoindentation tests and the stress–depth curve can be used to efficiently identify the depths of pop-in and pop-out. The PET/ITO specimen with 2% prestrain had the largest pop-in depth and the smallest pop-out depth.

Keywords: Prestrain; Carrier mobility; Band gap; Pop-in depth

1. Introduction

Indium–tin–oxide (ITO) films are widely used as a transparent conductor due to their high transparency to visible light and low electrical resistivity. They are used as transparent electrodes for various applications, such as displays (LCDs) and solar cells.

ITO films can be prepared by various deposition methods. Reactive sputter deposition is widely used for ITO film deposition [1–8]. Various glass materials have been used as the substrate of ITO films [1–6]. Post-deposition annealing has been conducted to investigate the effect of annealing temperature on the electrical, optical, and structural properties of ITO films [1]. The effects of sputtering pressure and substrate temperature on these properties have been characterized [2,3]. Films deposited at various deposition rates and gas compositions were investigated by Thilakan et al. [4]. The mechanical properties of the film, such as internal stress and adhesion, are important to pattern accuracy and durability [5]. Films prepared using pulsed magnetron sputtering have been compared to those prepared using direct-current (DC) sputtering [6]. The effects of pulsed magnetron sputtering parameters on film properties were also examined. The effects of the hydrogen gas ratio ($H_2/(H_2+Ar)$) on the electrical, optical, and mechanical properties were investigated by Kim et al. [7].

In the study of Park et al. [8], the crystallization behavior of ITO films prepared via radio-frequency (RF) magnetron sputtering

*Corresponding author at: 1 University Road, Tainan City 701, Taiwan (R. O.C.). Tel.: +886 6 2757575x62155.
E-mail address: jflin@mail.ncku.edu.tw (J.-F. Lin).

0272-8842/$ - see front matter © 2013 Elsevier Ltd and Techna Group S.r.l. All rights reserved.
http://dx.doi.org/10.1016/j.ceramint.2013.06.040

without external heating was examined. The difference in the crystallization between continuous and intermittent depositions was also investigated.

A high-resolution electron microscope (HREM) was used to clarify the structure of indium oxide films containing tin and tin oxides [9]. ITO film was composed of In_2O_3 and SnO. In the study of Hong and Han [10], ITO nanoparticles were synthesized by a gas evaporation process, and their physical properties, including crystal structure, were investigated. Tantalum-doped ITO films were deposited by co-sputtering with two-targets [11]. Tantalum doping strengthened the orientation of the (400) plane and resulted in a better crystalline structure, larger grain size, lower surface roughness, and better optical-electrical properties.

Transparent conductors on organic substrates have many applications. ITO films have been deposited onto polycarbonate (PC) substrates by RF magnetron sputtering. The influence of the oxygen content on film morphology and the electrical and optical properties of the film were investigated [12]. Both the refractive index and the extinction coefficient decrease with increasing oxygen content. The sheet resistance, optical transmittance, and microstructure of ITO films deposited on polymer substrates were studied [13]. Transmission electron microscopy (TEM) images showed dense growth close to the substrate and a sparse growth away from the substrate. Changes in the ITO film sheet resistance are correlated to the grain size and grain orientation. ITO films were deposited on a polypropylene adipate (PPA) substrate using bias RF magnetron sputtering. Good polycrystalline-structured ITO films with a low electrical resistivity have been obtained by applying a negative bias voltage to the substrate [14]. ITO thin films were grown by pulsed laser deposition on flexible poly(ethylene terephthalate) (PET) substrates. The structural, electrical, and optical properties of these films were investigated as a function of substrate deposition temperature and background gas pressure [15]. RF sputtering deposition was applied to deposit ITO on a PET substrate. The effects of deposition conditions on ITO film properties were examined [16]. The structural and optical properties of RF-magnetron-sputtered ITO films without in situ substrate heating and post-deposition annealing were investigated [17]. Oxygen deficiency was used to explain the loss of transmittance and the blackening of ITO films.

ITO films were prepared by a low-cost spray pyrolysis technique and their optical, structural, and electrical properties were investigated [18]. Low-sheet-resistance high-mobility films were obtained when the depositions were conducted at a substrate temperature of 520 °C. ITO films prepared on glass substrates from a mixture of In_2O_3 and SnO_2 were annealed [19]. The electrical and optical properties of the films were evaluated as a function of substrate temperature. Structural studies showed that the films were polycrystalline. The high-rate deposition of ITO thin films at a low substrate temperature was achieved using a facing target sputtering (FTS) system [20]. Thin films of ITO were deposited onto a PET substrate by reactive DC magnetron sputtering [21]. After coating, the PET substrate was annealed at a temperature of up to 175 °C. Shrinkage of the PET substrate initiated severe cracking in the film layer.

The mechanical properties of transparent conducting oxide thin films, including ITO, have been investigated [22,23]. The presence of hydrogen in a gas mixture during film deposition varied the hardness and elastic modulus of the ITO film significantly [22]. Five kinds of PET/aluminum-doped zinc oxide (AZO) specimen were prepared in our previous study to examine the effect of prestrain applied to the PET substrate before the coating of AZO film on the mechanical, optical, and electrical properties and morphology [23]. The film quality and optical and electrical properties of the film were also evaluated. This prestrain method is also applied in the present study.

In the present study, four kinds of PET/ITO specimen are prepared to examine the effect of prestrain applied to the PET substrate before the coating of ITO film on the mechanical, microstructure, optical, and electrical properties and surface morphology. The mold and four prestrains used in this study are exactly as same as those adopted in our previous study [24]. Nanoindentations with a function of electrical contact current are carried out to obtain the load–depth profiles, from which the hardness and Young's modulus are determined. The load–depth profile is turned to be the stress–depth curve. This stress–depth curve and the electrical current–depth curve are used to identify the depths of thin film pop-in and pop-out. Scanning electron microscopy (SEM) images of the porous ITO morphology are used to evaluate the void slenderness ratio as a function of prestrain. The lateral profiles of the ITO film are prepared by a focused ion beam (FIB) to observe the film thickness and the mean tilt angle of tubular voids. TEM morphologies of these lateral surfaces are used to determine the mean particle size of ITO deposited near the interface with the PET substrate. Electron diffraction (ED) patterns are used to determine the lattice style of the ITO crystallites. X-ray diffraction (XRD) patterns and Raman shifts are obtained to identify the primary lattices and the change in the residual stress due to the prestrain applied to the substrate. The relationship between d-spacing and the mean surface roughness of ITO film is established. The optical properties, namely transmittance, reflection, and absorption, are evaluated as functions of the prestrain. The absorption coefficient is thus evaluated and used to determine the optical (transition) band gap. The relationships among ITO particle size, optical band gap, carrier mobility and concentration, and mean absorption are thus established. The effect of the prestrain on ITO morphology and electrical resistance and the connection between the electrical current in nanoindentation tests and electrical resistance are investigated. The influences of material hardness and Young's modulus on the pop-in and pop-out depths of ITO film are discussed.

2. Specimen preparation

In the mass production of rollable and foldable electronics, a thin ceramic film coating on a soft, flexible substrate is efficiently deposited using a rotating deposition system, as shown in Fig. 1. The flexible substrate sheet is pressed against a rotating cylindrical drum, which is driven by frictional torque due to the

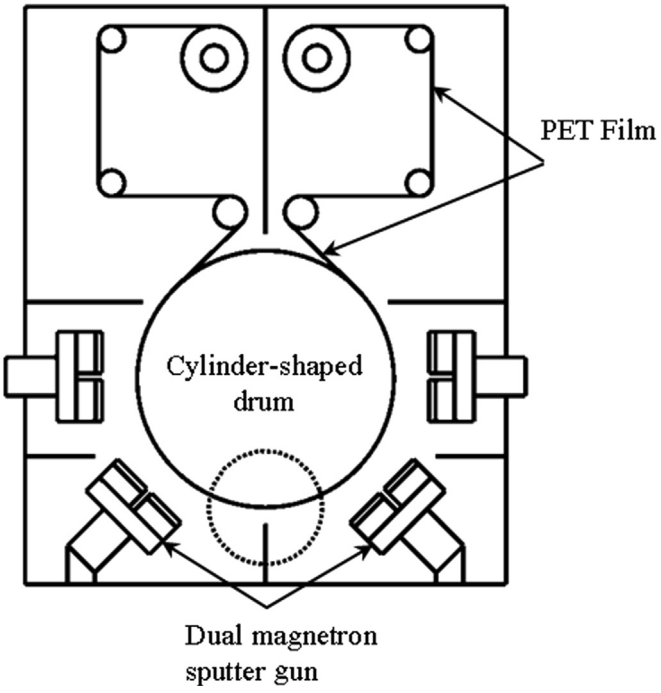

Fig. 1. Rotating deposition system [24].

Table 1
Basic physical and mechanical properties of poly(ethylene terephthalate) (PET). [25].

Thickness (μm)	188
Density (g/cm^3)	1.33
Tensile yield strength (MPa)	57–59
Tear strength (kN/m)	54–59
Specific heat capacity(J/kg °C)	1100
Haze (%)	0.8
Ratio of transmission (%, visible)	89
Young's modulus in *X*-direction (MPa)	3900
Young's modulus in *Y*-direction (MPa)	3900
Young's modulus in *Z*-direction (MPa)	4700
Poisson's ratio in *X*–*Y* plane	0.41
Poisson's ratio in *Y*–*Z* plane	0.31
Poisson's ratio in *X*–*Z* plane	0.39

tangential forces applied at the front and back sides of the moving PET substrate sheet belt. The material properties of PET are shown in Table 1. The ITO film is then deposited by magnetron sputter guns when the substrate sheet has rotated to the deposition positions. In order to mimic this deposition process, the mold shown in Fig. 2(a) was designed in this study. A schematic diagram of the mold is shown in Fig. 2(b). In this rig, the rectangular plate with a partial-arc top surface is fixed at the central region of the circular flat plate by a screw. The radius of curvature of the partial-arc top surface was designed to be as same as that shown in Fig. 1, which was measured as 50 cm. A rectangular PET (Shinpex, C87R8H, Taiwan) sheet (60 mm (length) × 50 mm (width) × 0.188 mm (thickness)) was held at its two ends by the two clamps such that the sheet specimen remained fixed on the partial-arc plate. The PET specimen can be elongated to produce various strains by adjusting a screw while remaining symmetrical with respect to the central line of the rectangular plate. The original length of the specimen before the tension force is applied is defined as L_0. The specimen is then elongated to a length L after the tension force is applied. The strain (ε) created in the specimen is defined as $(1-L_0/L) \times 100\%$. Four strain values, including no strain (0% strain), were selected in the present study to investigate the strain effect on the coating quality of the ITO film. The device shown in Fig. 2(a) with a PET sheet specimen was installed in the chamber of a DC magnetron sputtering system (Helix HLLS-87, Taiwan) after a strain was applied to deposit the ITO film.

The device with a PET sheet specimen was installed in the chamber of a DC magnetron sputtering system after a strain was applied. Transparent conductive oxide films with an area of 30 mm (length) × 50 mm (width) were deposited with ITO targets at a sputtering power of 100 W at room temperature for 2 h. The average thicknesses of the ITO films were 1459, 1443, 1452, and 1508 nm for corresponding to specimens with prestrain of 0%, 2%, 4%, and 6%, respectively. The material properties of ITO film are shown in Table 2. During the sputtering process, the solid temperature of the substrate surface increased from 20 °C to about 55 °C within first 60 min in the deposition process, and then became asymptotic to about 60 °C for the next 60 min. The heat distortion temperature of the PET

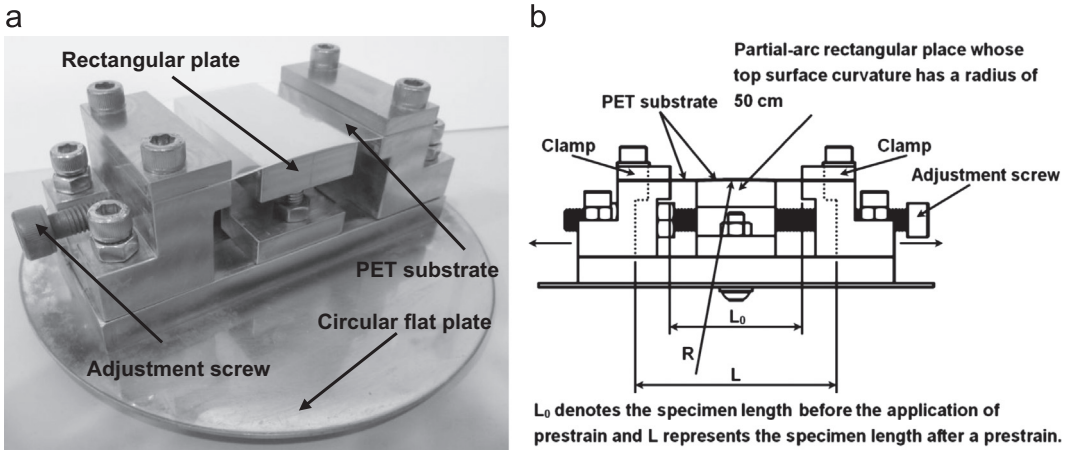

Fig. 2. (a) Photograph of mold and PET substrate and (b) schematic diagram of mold [24].

substrate was about 78 °C. The coefficient of thermal expansion (α) of the PET substrate is 20–25 ppm/°C. The temperature increase above the initial temperature was about 40 °C. The strain change $\Delta\varepsilon$ ($=\overline{\alpha}\Delta T$, where $\overline{\alpha}$ is the coefficient of thermal expansion of the PET substrate) is estimated to be 8×10^{-4}–10×10^{-4}. The effect of generated heat on the strain behavior of the film and substrate is thus very small.

3. Results and discussion

The topographies of the PET/ITO specimens with 0%, 2%, 4%, and 6% substrate prestrains are shown in Fig. 3(a), (b), (c) and (d), respectively. Crystalline porous materials were created in strip form with various slenderness ratios. The mean slenderness ratio decreased with increasing PET prestrain. These crystallites piled up in random orientations, resulting in the shape of porosities in the ITO film to be strongly dependent upon the prestrain. The lateral profile of the porous ITO films was prepared by using a focused ion beam (FIB). The morphologies of the specimens at the top surface of the ITO film and the region near the interface of the ITO film and the PET substrate were observed. As Fig. 4(a)–(d) shows, the porosities in the ITO film had a tubular form with a variable width decreasing from the top surface to the bottom surface of the ITO film. The tilt angle (θ) is defined as the angle between the vertical surface and the lateral surface of the tubule. The values of the ITO film thickness (t_f) and the tilt angle (θ) for the specimens are shown in Table 3. The magnitudes of these two parameters show the sequences: $(t_f)_{0\%} < (t_f)_{6\%} < (t_f)_{4\%} < (t_f)_{2\%}$ and $(\theta)_{0\%} \cong (\theta)_{6\%} < (\theta)_{4\%} < (\theta)_{2\%}$. The tilt angle of the tubular porosity is proportional to the film thickness, implying that the increase in the width of the tubular porosities is more significant than that in the film thickness. Nanoindentations were carried out to evaluate the hardness (H) and the reduced elastic modulus (Er) of the PET/

Table 2
Basic physical and mechanical properties of ITO film.

Physical property	Value
Density (g/cm^3)	6.8
Young's modulus (GPa)	116
Poisson's Ratio	0.35
Tensile failure strain (%)	2.2

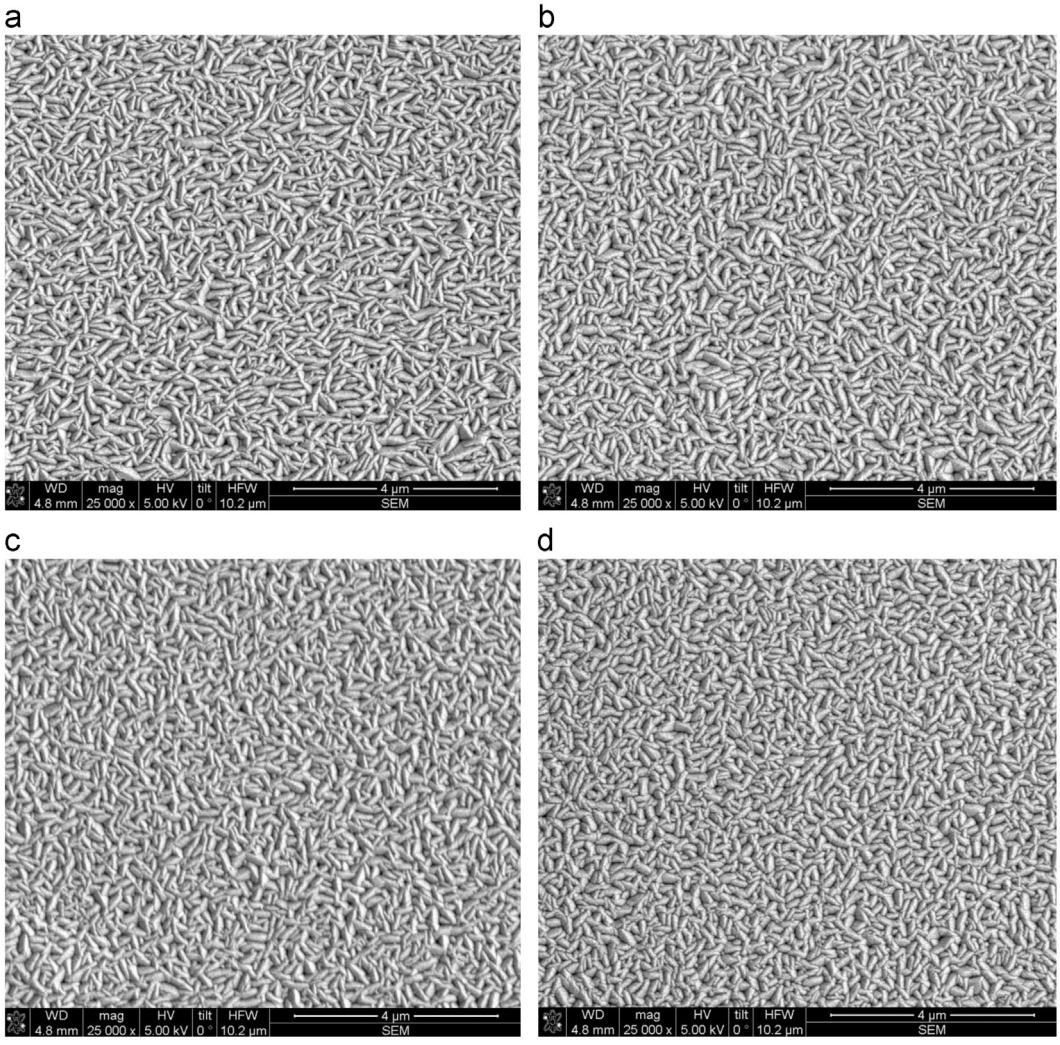

Fig. 3. SEM images of (a) PET-0%/ITO, (b) PET-2%/ITO, (c) PET-4%/ITO, and (d) PET-6%/ITO specimens.

Table 3
Experimental results of ITO film for the four coated specimens.

Specimens	Film thickness, t_f (nm)	Tilt angle, θ (°)	Er (GPa)	H (GPa)	Ra (nm)	FWHM (°)	Carrier mobility (cm^2/Vs)	Carrier concentration (cm^{-3})	XRD peak θ* (°)	d-spacing, a (Å)
PET-0%/ITO	5847 ± 64	0.58 ± 0.074	2.368	0.522	50.1 ± 9.30	0.39	1.7386	3.326×10^{20}	30.40	1.5222
PET-2%/ITO	6360 ± 46	0.75 ± 0.063	1.112	0.557	27.2 ± 0.95	0.99	0.5851	6.390×10^{20}	30.43	1.5208
PET-4%/ITO	6290 ± 56	0.66 ± 0.055	2.566	0.524	29.2 ± 1.48	1.15	1.2646	2.410×10^{20}	30.43	1.5208
PET-6%/ITO	6030 ± 20	0.58 ± 0.063	2.939	0.514	37.7 ± 4.20	1.15	1.7835	1.390×10^{20}	30.43	1.5211

FWHM: full width at half maximum.

ITO specimens. The values of these two parameters are shown in Table 3. They show the sequences:$(H)_{6\%} < (H)_{0\%} < (H)_{4\%} < (H)_{2\%}$ and $(Er)_{2\%} < (Er)_{0\%} < (Er)_{4\%} < (Er)_{6\%}$. The effect of the pretrain in the PET substrate on the hardness parameter is quite small. However, increases in both the tilt angle (θ) and the thickness (t_f) of the ITO film result in a reduction of the elastic modulus.

The TEM morphology of the specimen lateral cross section near the interface of the ITO film and the PET substrate was investigated. The ITO particle size was determined by inputting the TEM images into "Solidworks" software via the "Drawing" code. Then, the images were magnified to have their maximum size have nanometer resolution. The brightness and contrast were then adjusted to make the particles clearly visible. Then, the "Spline" code was used to measure the particle size. The reported particle sizes are the mean values of five readings obtained from five areas. The mean sizes of the ITO particles deposited near the interface were obtained as 41 ± 3.0, 15 ± 0.7, 13 ± 0.5, and 11 ± 0.3 nm for the samples with 0%, 2%, 4%, and 6% prestrains, respectively. This magnitude sequence for particle size is similar to that shown in the tilt angle (θ) if a nonzero prestrain is applied. This can be explained by the fact that the tilt angle of an ITO tubule is readily increased when the mean size of particles deposited onto a fixed area increases. The Scherrer equation was used to calculate the rough mean size (diameter, *Dia*) of the crystalline grains. The diameters for 0%, 2%, 4%, and 6% prestrains are 41.75, 16.48, 14.19, and 14.19 nm, respectively. The particle size predicted by this equation is fairly close to that obtained from the TEM images mentioned previously although the deviation increased with increasing PET prestrain.

Fig. 5(a)–(d) shows the ED patterns of ITO films deposited on PET-0%, PET-2%, PET-4%, and PET-6% substrates, respectively. In each of these figures, two ED patterns are provided for the ITO film near the protective Pt layer and near the PET substrate respectively. The (420), (622), (431), and (633) lattices were composed of In_2O_3 [9]. In each specimen, the clarity of the ED pattern near the top surface of the ITO film is higher than that near the PET substrate. However, the same crystalline lattices were created in these four specimens, irrespective of the prestrain applied in the PET substrate. Fig. 6 shows the XRD pattern of Fig. 5 for the one near the top surface of the ITO film. The microstructure in all these specimens is composed of the (622), (633), (420), and (134) lattices. The intensity of (622) is much higher than those of the other three lattices. In general, In_2O_3 has tetragonal and hexagonal crystallites as its microstructure. The former is a stable crystallite at atmospheric conditions. The (622) peak intensities (EDI) of these specimens show the sequence: $(EDI)_{0\%} < (EDI)_{6\%} \cong (EDI)_{4\%} < (EDI)_{2\%}$. The relationship between the EDI value and the electrical current created under a constant electrical voltage applied in the electrical contact resistance measurement is discussed in a later section.

The radius of curvature (R_0) for the PET substrate before the coating of the thin film was 5.455×10^6 μm. Average radii of curvature (R_s) of 3.529×10^5, 2.700×10^5, 2.341×10^5, and 1.833×10^5 μm, were obtained for PET-0%/ITO, PET-

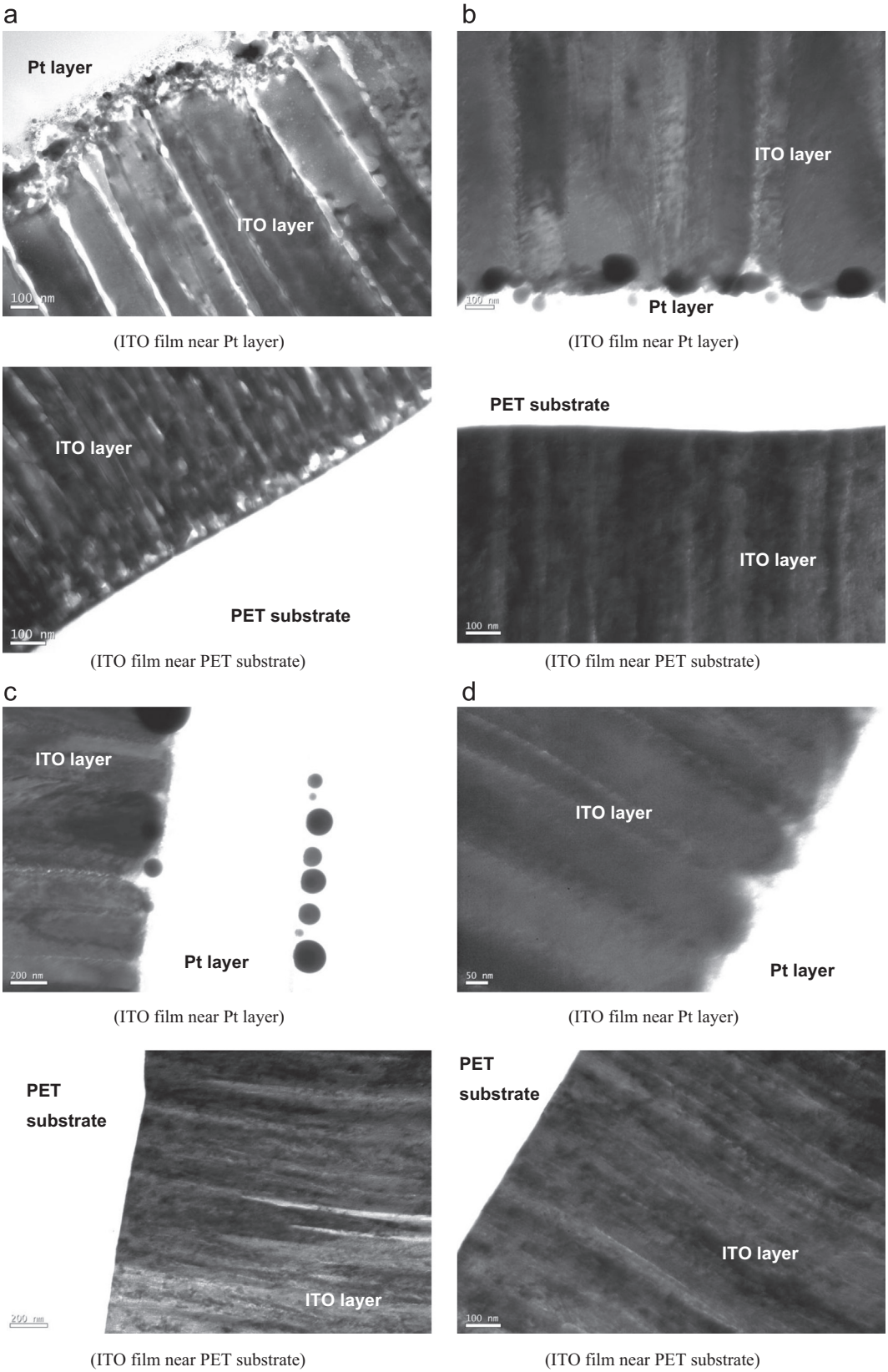

Fig. 4. SEM micrographs of the lateral surface of (a) PET-0%/ITO, (b) PET-2%/ITO, (c) PET-4%/ITO, and (d) PET-6%/ITO specimens.

2%/ITO, PET-4%/ITO, and PET-6%/ITO, respectively. The radius values are the mean values of three readings obtained from three areas. The as-received PET specimen (without an ITO coating) had the highest radius of curvature. For ITO films deposited on the PET substrate, the mean radius of curvature decreased with increasing applied strain to the substrate. The

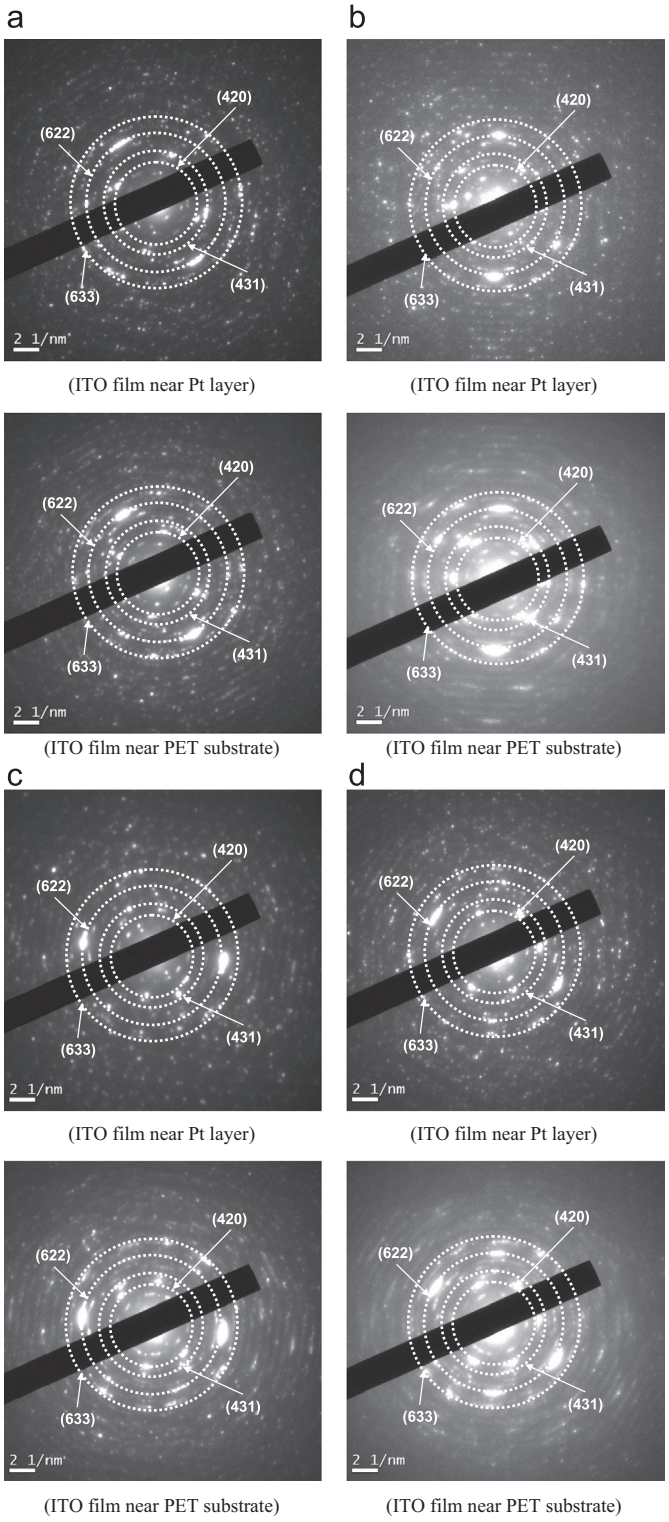

Fig. 5. ED patterns of ITO film near the protective Pt layer and near the PET substrate for (a) PET-0%/ITO, (b) PET-2%/ITO, (c) PET-4%/ITO, and (d) PET-6%/ITO.

Stoney formula [26] is:

$$\sigma_f = \frac{E_s t_s^2}{6t_f(1-\nu_s)}\left(\frac{1}{R_s}-\frac{1}{R_0}\right) \quad (1)$$

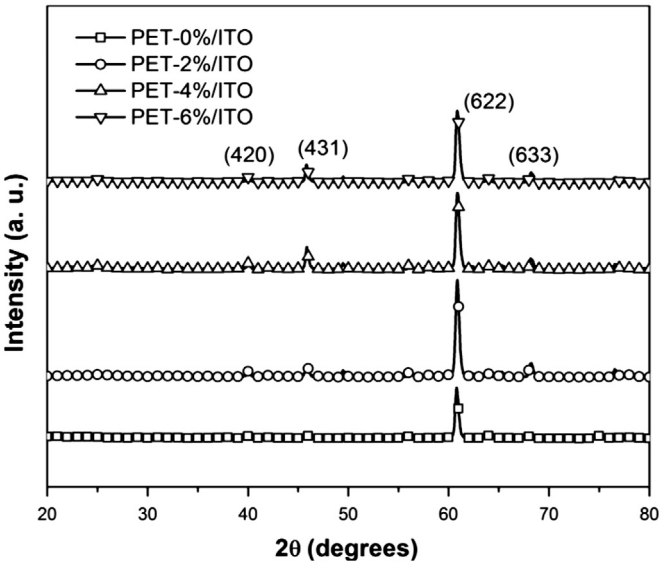

Fig. 6. XRD patterns of the four specimens.

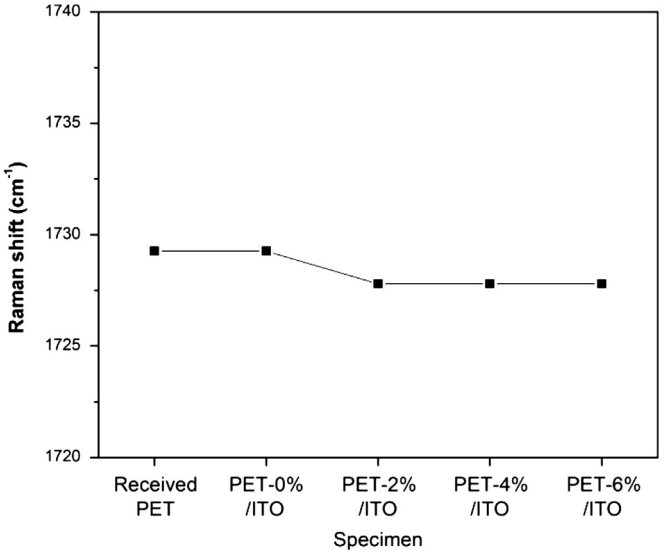

Fig. 7. Raman spectra of the four specimens.

where E_s is the elastic modulus of the PET substrate; $t_s$is the thickness of the PET substrate; t_f is the thickness of the ITO film; and $\nu_s(=0.43)$ is Poisson's ratio of the PET substrate. Average compressive residual stresses of the ITO film of −72, −96, −111, and −138 MPa were obtained for PET-0%/ITO, PET-2%/ITO, PET-4%/ITO, and PET-6%/ITO, respectively. The average residual stress for each of these four specimens was obtained from three readings. The compressive residual stress significantly increased with decreasing radius of curvature of the PET substrate.

Fig. 6 shows the XRD patterns of the four specimens. Before the application of a prestrain (PET-0%/ITO), the $2\theta^*$ value of the (622) lattice was 60.80°. With a nonzero prestrain applied to the PET substrate, the $2\theta^*$ values corresponding to the (622) diffraction peak of specimens with 2%, 4%, and 6% prestrains increased to a value close to 60.86°. This means that the

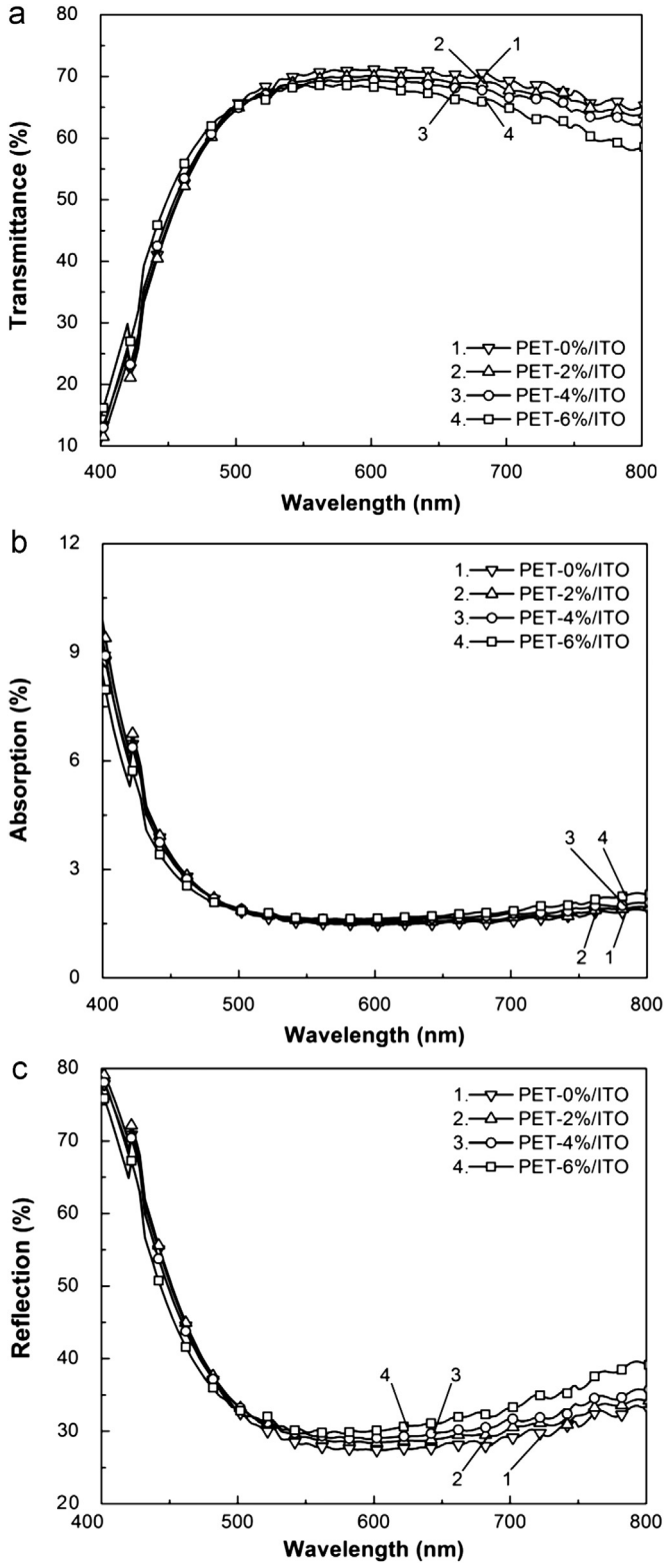

Fig. 8. (a) Transmittance, (b) absorption, and (c) reflection data as functions of wavelength and prestrain.

compressive residual stress in the specimens increased when a nonzero prestrain was applied to the PET substrate. The sequence of $(2\theta^*)_{0\%} < (2\theta^*)_{6\%} \cong (2\theta^*)_{4\%} \cong (2\theta^*)_{2\%}$ was obtained although the variance in $2\theta^*$ due to the prestrain is quite narrow. Blue shifts are created in the specimens due to the application of a nonzero prestrain. Therefore, compressive stresses formed in the PET/ITO specimens with nonzero prestrain are quite close each other, and they are slightly higher than that of PET-0%/ITO.

The combined effect of a larger film thickness and a higher tilt angle of the ITO film created in the nonzero prestrain specimens was compared to that in the specimens with zero prestrain. Fig. 7 shows the Raman shifts for the four PET substrates. The three main peaks for the PET-0%/ITO specimen occur at 1292, 1616, and 1729 cm^{-1}. Fig. 7 also shows the Raman shift values of the five specimens, including the as-received PET substrate. They were obtained from the highest peaks in each Raman spectrum. The results indicate that the Raman shifts for the PET substrates with a nonzero prestrain are only slightly smaller than that of PET-0%/ITO (1729 cm^{-1}). The wavenumber sequence of the Raman shift is the same as that of d-spacing. This behavior indicates that the compressive stress in the ITO film is increased by the prestrain. The compressive stress for the specimens with a nonzero prestrain was almost invariant with the prestrain value.

The d-spacing (a) was evaluated using the expression, $a = \lambda/(2 \sin \theta^*)$, where the θ^* angles for the four prestrains were obtained from the $2\theta^*$ angles corresponding to the (622) peaks of the XRD patterns shown in Fig. 6, and $\lambda = 10.117$ Å for ITO film. The values in Table 3 were obtained from the evaluations of the (622) peaks in the coated specimens. The sequence of the mean surface roughnesses (Ra) for the four specimens is the same as that for d-spacing ($(a)_{2\%} \cong (a)_{4\%} < (a)_{6\%} < (a)_{0\%}$). It is thus reasonable to assume that the mean surface roughness of the specimen is related to the d-spacing. A nonzero prestrain applied to the substrate reduced both the d-spacing and the mean surface roughness of the ITO films. It is also found that a specimen with a low value of d-spacing is helpful to increase its hardness.

The wavenumbers for the four PET/ITO specimens are 1729.27, 1727.8, 1728.0, and 1728.1 cm^{-1}. The sequence of the Raman blue-shift is the same as that for d-spacing (a) shown in Table 3 ($(a)_{2\%} \cong (a)_{4\%} < (a)_{6\%} < (a)_{0\%}$). Regarding the shape difference in the Raman spectra, an increase in the prestrain applied to the PET substrate led to neighboring disorder and local geometric disorientation, affecting the Raman bending- and stretching-mode vibrations, as suggested by the molecular theory of vibration. The Raman bands narrowed slightly with increasing prestrain applied to the PET substrate.

The optical transmittance spectra of the ITO films deposited on PET substrates are shown in Fig. 8(a). The films are fairly transparent in the visible-light range. An increase in the prestrain increased the transmittance (T) of the PET/ITO specimens in the light wavelength range of 400–500 nm, but reduced the transmittance in the light wavelength range of >500 nm. The transmittance of the PET/ITO specimens is strongly dependent upon the band gap and carrier concentration. The band gap of In_2O_3 is 3.7 eV. In the wavelength region of <380 nm (ultraviolet rays), the energy of photons is higher than 3.7 eV. The excited photons in the wavelength range of <335 nm (absorption edge, E) have high absorption and thus low transmittance. In the wavelength

Table 4
Values of optical properties for specimens with various prestrains.

Prestrain (%)	Absorption, *Ab* (%) (400–800 nm)	Transmittance, *T* (%) (400–800 nm)	Reflection, *Re* (%) (400–800 nm)
0	2.3 ± 1.54	62.4 ± 14.39	35.4 ± 12.88
2	2.4 ± 1.63	61.3 ± 14.46	36.3 ± 12.87
4	2.4 ± 1.49	61.1 ± 13.54	36.6 ± 12.09
6	2.3 ± 1.27	60.4 ± 12.01	37.3 ± 10.76

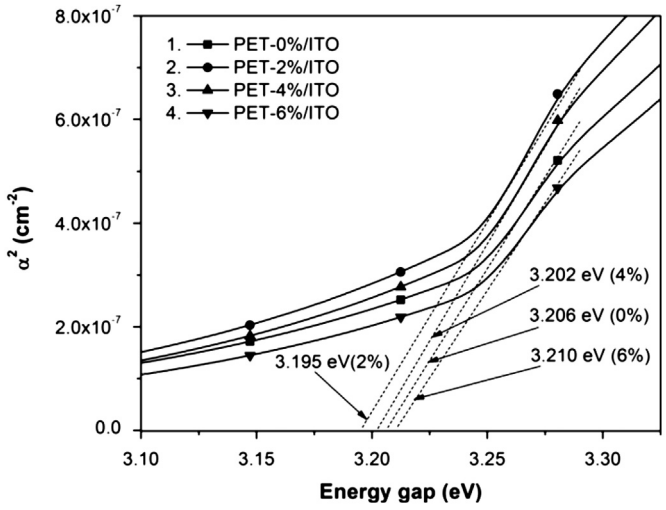

Fig. 9. Band gap energy of the four specimens.

range from 380 nm (visible light) to 800 nm (near-infrared rays), the excited photons have low absorption and therefore high transmittance. In this study, the absorption edge $E = hC_0/\lambda$ due to the energy band gaps for the four specimens shows the sequence: $(E)_{6\%} < (E)_{0\%} < (E)_{4\%} < (E)_{2\%}$. Similarly, the absorption edge due to the carrier concentration shows the sequence: $(E)_{6\%} < (E)_{4\%} < (E)_{0\%} < (E)_{2\%}$. The combined effect of these two absorption edges causes the mean absorption (*Ab*) of the specimens (see Table 4) to have the following sequence in the visible light region (400–800 nm): $(Ab)_{6\%} \leq (Ab)_{0\%} \leq (Ab)_{4\%} \leq (Ab)_{2\%}$. Fig. 8(b) shows the absorption spectra of the four specimens. These absorption curves have a concave form in the wavelength range of 400–800 nm. In the wavelength range of roughly > 500 nm, the absorption increased with increasing prestrain applied to the substrate. In the wavelength range of < 500 nm, the absorption behavior is opposite to that described above. Fig. 8(c) shows the reflection spectra. The behavior demonstrated by reflection is similar to that of absorption. PET-0%/ITO has the highest transmittance and the lowest absorption. The mean values of the optical parameters of the four specimens are shown in Table 4. Increasing the prestrain in the PET substrate reduced the mean transmittance (*T*) slightly and thus increased the mean reflectance (*Re*). Of note, an increase in the particle size slightly decreased the transmittance (*T*) and thus increased the reflectance (*Re*). The absorption coefficient (α) can be calculated as [27]:

$$\alpha = \ln(1/T)/t_f \tag{2}$$

where *T* denotes transmittance and t_f denotes film thickness. The optical (transition) band gap, *Eg*, which depends on the absorption coefficient, (α), can be written as [28]:

$$(\alpha h\nu)^2 = A(h\nu - Eg) \tag{3}$$

where *A* is a constant. *Eg* can be determined by extrapolating the linear portion of the curve to intersect the $h\nu$ axis. Fig. 9 shows the variations of α^2 with photon energy. The *Eg* values obtained from extrapolations for the four PET/ITO specimens are also shown. The results show the sequence: $(Eg)_{2\%} < (Eg)_{4\%} < (Eg)_{0\%} < (Eg)_{6\%}$. This *Eg* sequence is opposite to that shown by the mean particle size of ITO deposited at the interface of the ITO film and PET substrate. It is thus concluded that the increase in the ITO particle size caused the reduction of the optical band gap (*Eg*) and the increase in the mean absorption. The carrier mobility and concentration and electrical resistance were obtained as functions of the substrate prestrain. The carrier mobility (*Mb*) values are shown in Table 3. They show the sequence: $(Mb)_{2\%} < (Mb)_{4\%} < (Mb)_{6\%} < (Mb)_{0\%}$. This sequence resembles that shown by the optical band gap (*Eg*) (Fig. 9) except that the order of specimens with prestrain of 0% and 6% is reversed. The difference in both *Mb* and *Eg* between the specimens with the prestrain of 0% and 6% is actually quite small. These two parameters are thus related; a specimen with a large *Eg* value is apt to have a high *Mb* value. The carrier concentration (*Cc*) values (see Table 3) of the four specimens show the sequence: $(Cc)_{6\%} < (Cc)_{4\%} < (Cc)_{0\%} < (Cc)_{2\%}$. This sequence is opposite to that shown by Young's modulus (*Er*). That is, a PET/ITO specimen with a higher Young's modulus has a lower carrier concentration. A higher carrier concentration in the specimen resulted in a lower carrier mobility when a nonzero prestrain was applied to the PET substrate.

In the present study, nanoidentations with a function of electrical contact resistance (ECR) were carried out on a nanotester (Hysitron TI700 UBI, USA). The load–depth and electrical current–depth profiles for the entire indentation process were thus available. The curves are shown in Fig. 10 (a), (b), (c) and (d) for specimens with prestrains of 0%, 2%, 4%, and 6%, respectively. The electrical current–depth profile were used to identify the depths corresponding to the pop-in in the loading process and the pop-out in the unloading process, and the electrical current at the maximum indentation depth. In the loading process, a significant rise in the electrical current led to a noticeable increase in the contact area of the indenter with the ITO film as pop-in occurred. The pop-in depth ($D_{pop\text{-}in}$) parameter shows the sequence: $(D_{pop-in})_{4\%} \leq (D_{pop-in})_{6\%} < (D_{pop-in})_{0\%} < (D_{pop-in})_{2\%}$. The $D_{pop\text{-}in}$ values are denoted by the vertical line "————" in Fig. 10. This sequence is related to the specimen's hardness and Young's modulus.

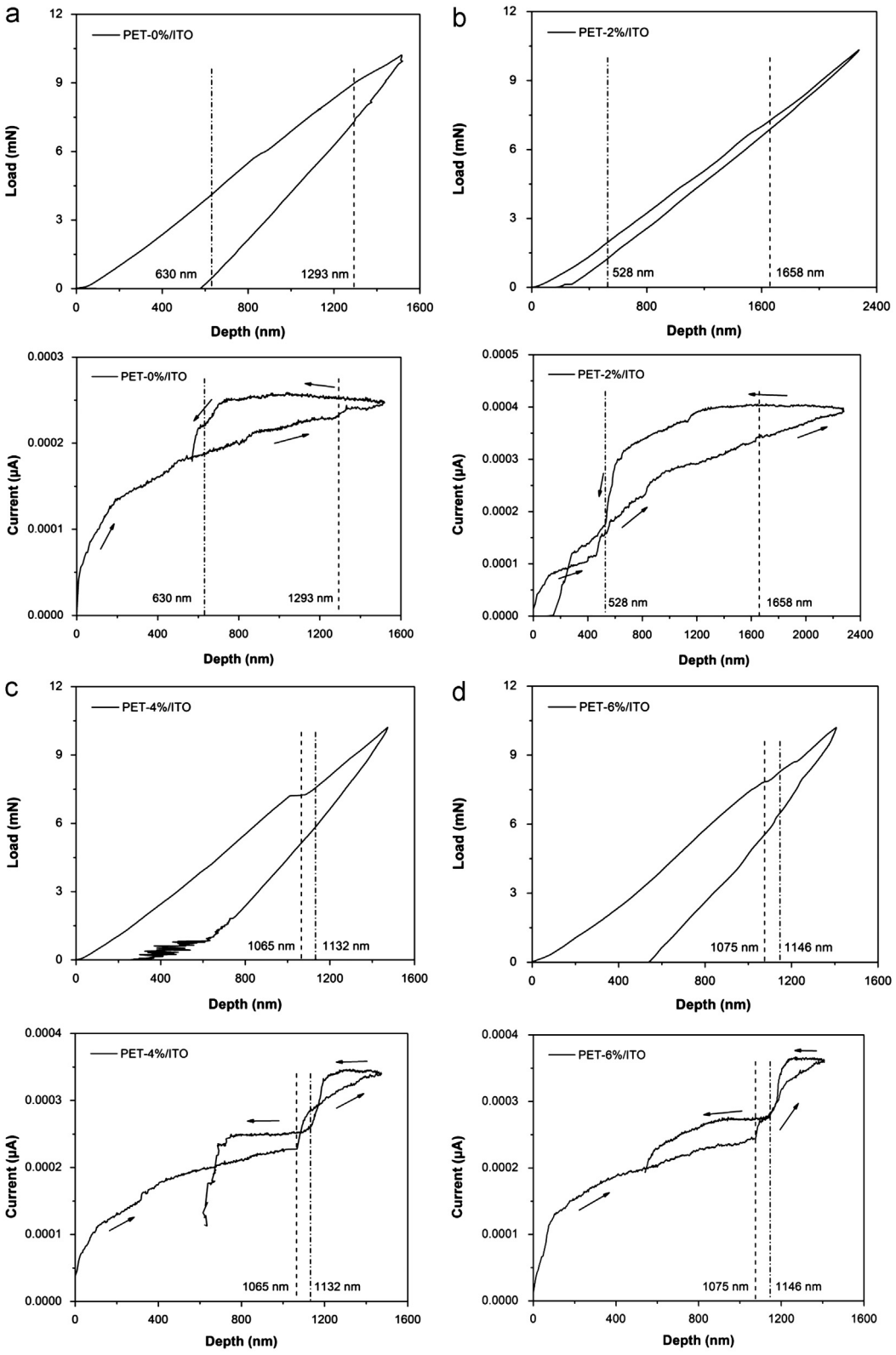

Fig. 10. Load–depth and electrical current–depth curves obtained from the nanoindentations of (a) PET-0%/ITO, (b) PET-2%/ITO, (c) PET-4%/ITO, and (d) PET-6%/ITO.

A specimen with a high hardness and a low Young's modulus will have a large pop-in depth. Pop-out occurred in the unloading process with a significant decrease in the indentation depth, thus resulting in a noticeable decrease of electrical current. The pop-out depth ($D_{pop\text{-}out}$) (symbolized by "————" in Fig. 10) arising in the unloading process shows the sequence: $(D_{pop-out})_{2\%} \leq (D_{pop-out})_{0\%} < (D_{pop-out})_{4\%} < (D_{pop-out})_{6\%}$. This sequence is the same as that of Young's

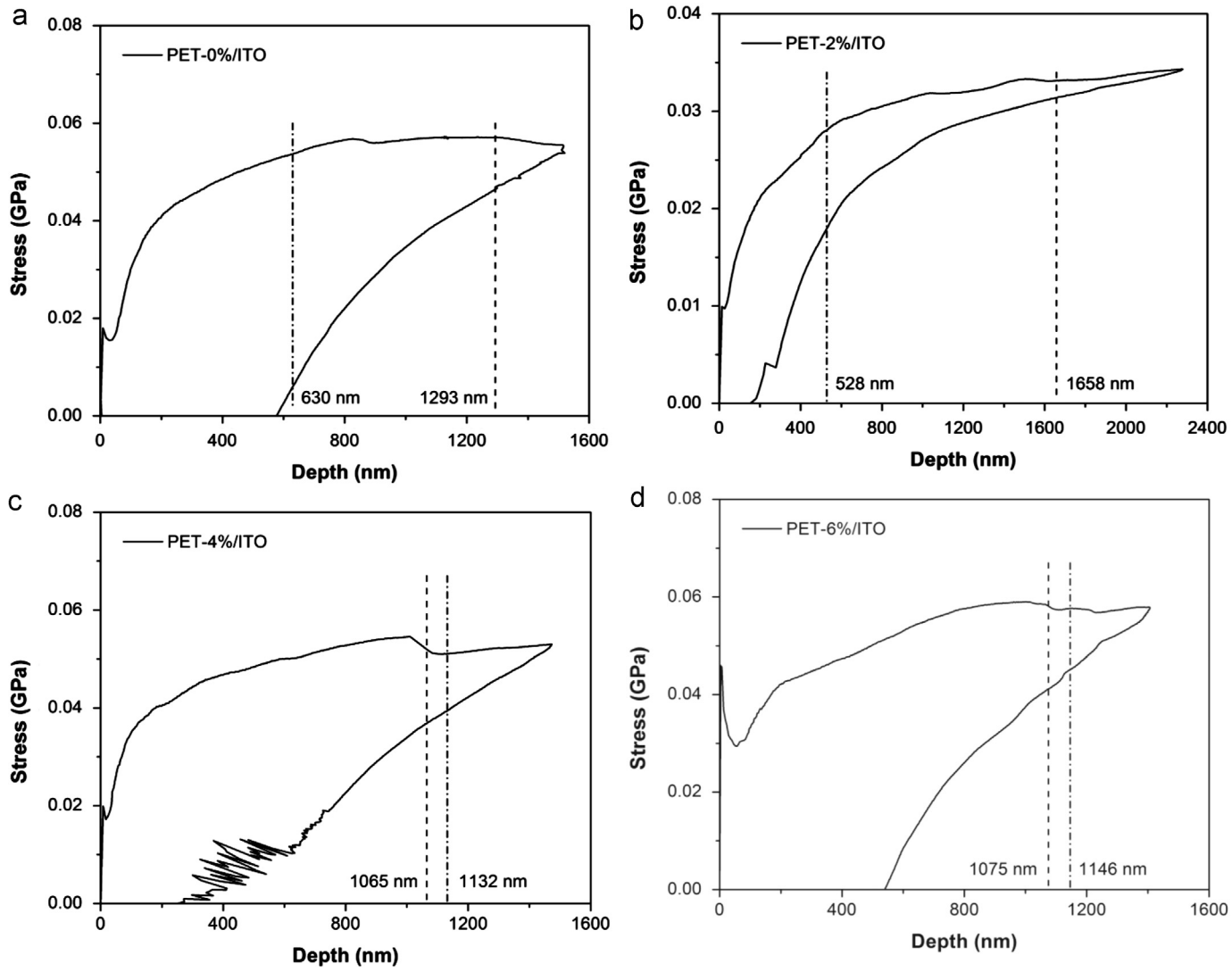

Fig. 11. Stress–depth curves obtained from the nanoindentations of (a) PET-0%/ITO, (b) PET-2%/ITO, (c) PET-4%/ITO, and (d) PET-6%/ITO.

modulus (*Er*). It is thus concluded that increasing Young's modulus of a specimen and decreasing its hardness can cause pop-out to arise at a larger indentation depth in the unloading process. The sequences of $D_{pop\text{-}in}$ and $D_{pop\text{-}out}$ indicate that a specimen with a larger $D_{pop\text{-}in}$, often but not always, has a smaller $D_{pop\text{-}out}$. The PET-2%/ITO specimen had the largest pop-in depth as well as the smallest pop-out depth due to it having the highest hardness and the lowest Young's modulus. The electrical current (I) measured at the maximum indentation depth shows the sequence: $(I)_{0\%} < (I)_{4\%} < (I)_{6\%} < (I)_{2\%}$. The electrical resistance (R) values show the sequence: $(R)_{2\%} < (R)_{6\%} \leq (R)_{4\%} < (R)_{0\%}$. The sequence exhibited by the electrical current (I) is opposite to that of electrical resistance (R). This indicates that a proper nonzero prestrain applied to the PET substrate can effectively reduce the electrical resistance of the ITO film. A comparison of the sequence of electrical resistance to that of mean surface roughness (*Ra*) indicates that a specimen with a rough surface will have a high electrical contact resistance. The sequence of *EDI* (the (622) peak intensity) due to the difference in the prestrain is found fairly close to the sequence of I except the difference in order between the prestrains of 4% and 6%. A specimen with a larger value of *EDI* is seemingly helpful to have a high electrical current.

The load–depth curves shown in Fig. 10 can be used to obtain the stress–depth curves following the method described in the study of Li et al. [29]. Fig. 11(a)–(d) shows the stress–depth profiles for the four specimens, respectively. These profiles can be effectively used to identify the pop-in depth of a specimen, especially in the case of having the evidence still ambiguous to verify this behavior. The pop-in stress in the loading process is almost invariant with increasing indentation depth [29]. As shown in Figs. 10 and 11, the pop-in electrical current for the specimens with a small prestrain does not exhibit a significant change. However, the stress at the pop-in depth was almost unchanged until the maximum indentation depth was reached. It is thus concluded that the combination of the electrical current–depth curve and the stress–depth curve can be used to efficiently identify the depths of pop-in and pop-out arising in the loading and unloading processes, respectively.

4. Conclusions

1. The prestrain applied to a PET substrate causes the crystalline porosity of the ITO film to be in strip form with various slenderness ratios. The mean slenderness ratio decreases with increasing prestrain. The porosity in the ITO film is in tubule form with width that varies with film depth. The tilt angle of a tubular porosity is proportional to the film thickness. Increases in both the tilt angle and the thickness of ITO film result in a reduction of the elastic modulus. The tilt angle is increased due to an increase in the particle size of ITO deposited on the PET substrate.
2. Due to the combined effect of larger ITO film thickness and higher tilt angle in specimens with a nonzero prestrain, the compressive residual stress in the these specimens is higher than that in the specimen with zero prestrain in the substrate.
3. The sequence of the mean surface roughness for the specimens with various prestrains is as same as that exhibited by the d-spacing. A nonzero prestrain applied to the substrate reduces both the d-spacing and the mean surface roughness of the ITO film. A specimen with a smaller d-spacing is advantageous to have a higher hardness.
4. The transmittance of the PET/ITO specimens depends on the band gap and carrier concentration of the ITO film. Increasing the substrate prestrain decreases the mean transmittance, but increases the mean reflectance of the PET/ITO specimens. An increase in ITO particle size results in the reduction of the optical band gap (*Eg*). A decrease in the ITO particle size increases transmittance and decreases reflection.
5. PET/ITO specimens with a large optical (transition) band gap (*Eg*) are apt to have a high carrier mobility (*Mb*). A specimen with a high Young's modulus has a low carrier concentration. A high carrier concentration results in a low carrier mobility if a nonzero prestrain is applied. A nonzero prestrain leads to the creation of a smooth ITO film with low electrical resistance. Electrical current is inversely proportional to electrical resistance.
6. Decreasing Young's modulus of a specimen and increasing the specimen's hardness increases the pop-in depth and decreases the pop-out depth. The PET-2%/ITO specimen had the largest pop-in depth and the smallest pop-out depth.

References

[1] L.J. Meng, A. Maçarico, R. Martins, Study of annealed indium tin oxide films prepared by rf reactive magnetron sputtering, Vacuum 46 (1995) 673–680.

[2] L.J. Meng, M.P. Dos Santos, Properties of indium tin oxide (ITO) films prepared by r.f. reactive magnetron sputtering at different pressures, Thin Solid Films 303 (1997) 151–155.

[3] L.J. Meng, M.P. Dos Santos, Properties of indium tin oxide films prepared by rf reactive magnetron sputtering at different substrate temperature, Thin Solid Films 322 (1998) 56–62.

[4] P. Thilakan, C. Minarini, S. Loreti, E. Terzini, Investigations on the crystallisation properties of RF magnetron sputtered indium tin oxide thin films, Thin Solid Films 388 (2001) 34–40.

[5] T. Sasabayashi, N. Ito, E. Nishimura, M. Kon, P.K. Song, K. Utsumi, A. Kaijo, Y. Shigesato, Comparative study on structure and internal stress in tin-doped indium oxide and indium–zinc oxide films deposited by r.f. magnetron sputtering, Thin Solid Films 445 (2003) 219–223.

[6] M.S. Hwang, H.J. Lee, H.S. Jeong, Y.W. Seo, S.J. Kwon, The effect of pulsed magnetron sputtering on the properties of indium tin oxide thin films, Surface and Coatings Technology 171 (2002) 29–33.

[7] D.G. Kim, S. Lee, G.H. Lee, S.C. Kwon, Effects of hydrogen gas on properties of tin-doped indium oxide films deposited by radio frequency magnetron sputtering method, Thin Solid Films 515 (2007) 6949–6952.

[8] J.O. Park, J.H. Lee, J.J. Kim, S.H. Cho, Y.K. Cho, Crystallization of indium tin oxide thin films prepared by RF-magnetron sputtering without external heating, Thin Solid Films 474 (2005) 127–132.

[9] T. Nakao, T. Nakada, Y. Nakayama, K. Miyatani, Y. Kimura, Y. Saito, C. Kaito, Characterization of indium tin oxide film and practical ITO film by electron microscopy, Thin Solid Films 370 (2000) 155–162.

[10] S.J. Hong, J.I. Han, Synthesis and characterization of indium tin oxide (ITO) nanoparticle using gas evaporation process, Journal of Electroceramics 17 (2006) 821–826.

[11] B. Zhang, X. Dong, X. Xu, J. Wu, Preparation and characterization of tantalum-doped indium tin oxide films deposited by magnetron sputtering, Scripta Materialia 58 (2008) 203–206.

[12] W.F. Wu, B.S. Chiou, Deposition of indium tin oxide films on polycarbonate substrates by radio-frequency magnetron sputtering, Thin Solid Films 298 (1997) 221–227.

[13] A.K. Kulkarni, K.H. Schulz, T.S. Lim, M. Khan, Electrical, optical and structural characteristics of indium–tin–oxide thin films deposited on glass and polymer substrates, Thin Solid Films 308–309 (1997) 1–7.

[14] Z. Yang, S. Han, T. Yang, L. Ye, H. Ma, C. Cheng, ITO films deposited on water-cooled flexible substrate by bias RF Magnetron Sputtering, Applied Surface Science 161 (2000) 279–285.

[15] H. Kim, J.S. Horwitz, G.P. Kushto, Z.H. Kafafi, D.B. Chrisey, Indium tin oxide thin films grown on flexible plastic substrates by pulsed-laser deposition for organic light-emitting diodes, Applied Physics Letters 79 (2001) 284–286.

[16] F.L. Wong, M.K. Fung, S.W. Tong, C.S. Lee, S.T. Lee, Flexible organic light-emitting device based on magnetron sputtered indium–tin-oxide on plastic substrate, Thin Solid Films 466 (2004) 225–230.

[17] W.F. Wu, B.S. Chiou, S.T. Hsieh, Effect of sputtering power on the structural and optical properties of RF magnetron sputtered ITO films, Semiconductor Science Technology 9 (1994) 1242–1249.

[18] K.S. Ramaiah, V.S. Raja, A.K. Bhatnagar, R.D. Tomlinson, R.D. Pilkington, A.E. Hill, S.J. Chang, Y.K. Su, F.S. Juang, Optical, structural and electrical properties of tin doped indium oxide thin films prepared by spray-pyrolysis technique, Semiconductor Science Technology 15 (2000) 676–683.

[19] J. George, C.S. Menon, Electrical and optical properties of electron beam evaporated ITO thin films, Surface and Coatings Technology 132 (2000) 45–48.

[20] Y. Hoshi, H.O. Kato, K. Funatsu, Structure and electrical properties of ITO thin films deposited at high rate by facing target sputtering, Thin Solid Films 445 (2003) 245–250.

[21] M. Boehme, C. Charton, Properties of ITO on PET film in dependence on the coating conditions and thermal processing, Surface and Coatings Technology 200 (2005) 932–935.

[22] K. Zeng, F. Zhu, J. Hu, L. Shen, K. Zhang, H. Gong, Investigation of mechanical properties of transparent conducting oxide thin films, Thin Solid Films 443 (2003) 60–65.

[23] T.C. Li, P.T. Hsieh, J.F. Lin, Effects of pre-strain applied at a polyethylene terephthalate substrate before the coating of Al-doped ZnO film on film quality and optical and electrical properties, Ceramics International 37 (2011) 2467–2476.

[24] T.C. Li, B.H. Wu, J.F. Lin, Effects of pre-strain applied at a polyethylene terephthalate substrate before the coating of TiO_2 film on the coating film quality and optical performance, Thin Solid Films 519 (2011) 7875–7882.

[25] S.L. Zhang, J.C.M. Li, Anisotropic elastic moduli and Poisson's ratios of a poly(ethylene terephthalate) Film, Journal of Polymer Science Part B: Polymer Physics 42 (2004) 260–266.

[26] G.G. Stoney, The tension of metallic films deposited by electrolysis, Proceedings of the Royal Society of London A82 (1909) 172–175.

[27] W.N. Miao, X.F. Li, Q. Zhang, L. Huang, Z.J. Zhang, L. Zhang, X.J. Yan, Transparent conductive In_2O_3:Mo thin films prepared by

reactive direct current magnetron sputtering at room temperature, Thin Solid Films 500 (2006) 70–73.

[28] V.R. Shinde, T.P. Gujar, C.D. Lokhande, R.S. Mane, S.H. Han, Mn doped and undoped ZnO films: a comparative structural, optical and electrical properties study, Materials Chemistry and Physics 96 (2006) 326–330.

[29] T.C. Li, C.F. Han, B.H. Wu, P.T. Hsieh, J.F. Lin, Effects of prestrain applied to a polyethylene terephthalate substrate before the coating of Al-doped ZnO film on film quality, electrical properties, and pop-in behavior during nanoindentation, Journal of Microelectromechanical Systems 21 (2012) 1059–1070.